Received: 13 February 2021 | Revised: 2 July 2021 | Accepted: 20 August 2021

IET Generation, Transmission & Distribution

DOI: 10.1049/gtd2.12295

The Institution of Engineering and Technology WILEY

ORIGINAL RESEARCH PAPER

HVDC grids stability improvement by direct current power system stabilizer

Neda Azizi[1] | **Hassan Moradi CheshmehBeigi**[1] | **Kumars Rouzbehi**[2]

[1] Department of Electrical Engineering, Razi University, Kermanshah, Iran

[2] Department of System Engineering and Automatic Control, University of Seville, Seville, Spain

Correspondence
Hassan Moradi CheshmehBeigi, Tagh-e-Bostan, University St., Kermanshah, Postal Code 6714414971, Iran.
Email: ha.moradi@razi.ac.ir

Abstract

High-voltage direct current breaker is among the essential components of high-voltage direct current grids. Such a breaker generally needs a direct current reactor to reduce the fault currents rate. However, direct current reactors have destructive effects on the multi-terminal high-voltage direct current grid dynamic stability, and in such a system, despite the variety of controllers, the system dynamics are highly sensitive to the operating point. Therefore, additional damping control will be needed. This paper proposes a modification to be applied to the traditional droop controller of high-voltage direct current grids to cope with the influence of these large reactors, improving the direct voltage stability and decreasing power variations in the transient events by introducing a direct current power system stabilizer. The proposed method for direct voltage control has been investigated through the analytical model of the system. Stability improvement has been studied following the application of the proposed method by investigating zeros, poles, and frequency response analysis. Moreover, a method is proposed for optimal design and optimal placement of direct current power system stabilizer. The system analysis and time-domain simulations demonstrate a decent damping improvement attained by the proposed method. All simulations and analytical studies are conducted on Cigré DCS3 test high-voltage direct current grid in MATLAB/Simulink.

1 | INTRODUCTION

The integration of renewable generations and the electrification of oil and gas platforms, as well as the incorporation of different electricity markets, has resulted in a request for new transmission system solutions [1]. Yet, high-voltage direct current (HVDC) transmission technology is used mainly for point-to-point transmission with a sending power converter station and a receiving power converter station [2,3]. In recent years, multi-terminal high-voltage direct current (MT-HVDC) transmission systems have been proposed primarily for use in offshore wind farms along with the classical system [4]. It is identified that the transient stability of such a grid is of serious concern under large disturbances [5] and additional control (to provide adequate damping to HVDC grids) would be necessary [5] and voltage regulation has a crucial role in the control of MT-HVDC grids [2].

Different strategies have been proposed to control and improve the stability of HVDC networks [6]. These strategies can be categorized into two types of conventional control methods and advanced intelligent control methods. In addition, in terms of stability oscillation, they can be classified into several categories of power/frequency oscillations, sub-synchronous oscillations, and direct current (DC) oscillations [7–10]. Mathematical modelling and AC/DC interaction analysis of HVDC systems are studied in [11]. The model of a voltage source converter-based HVDC (VSC-HVDC) system is extracted in [12], and DC voltage control and power-sharing in an HVDC system based on droop control are proposed in [13]. The effect of DC breakers on the stability of the HVDC system is investigated in [14], but the system under study is VSC based, also the effect of the proposed stabilizer on the performance of the droop controller is not investigated. Also, the modelling of overhead transmission lines and cables in [14]

is based on the π-section model, which is less accurate than modelling based on the model frequency-dependent model (FD-π) model [15,16]. However, addressing the problem of oscillations in HVDC system needs more effort yet [14] and none of them has investigated a combination of droop control and power system stabilizer (PSS) applied to the DC side of modular multi-level converters—based HVDC (MMC-HVDC) stations. The proposed supplementary controller in [17] applied to the DC side of the VSC converter and its parameters tuned by particle swarm optimization (PSO) algorithm considering VSC-HVDC and π line modelling. In [17], the VSC average model is used for converter modelling and the π-section model is used for the line modelling.

The main effort of control of DC voltage is to eliminate the imbalance of power in transient conditions and keep the voltage level within an acceptable limit. Therefore, this paper proposes an effective DC-voltage damping controller as direct current power system stabilizer (DC-PSS) to improve the overall system direct voltage/power stability in the presence of large reactors. This controller will have significant impacts on the grid stable operation under grid disturbances and leads to damping of low-frequency fluctuations. Also, to investigate the efficiency of the proposed method alongside the other controllers, several droop controllers are used in the understudy system. By utilizing the proposed controller, fluctuations of voltage and power in HVDC grids are suppressed. It occurs by injecting damping signals into the droop controller loop of the selected power converter stations in case of transient events. Besides, to achieve the proper performance of the DC-PSS, all parameters of DC-PSS are optimally tuned at the same time by a mixed-integer non-linear optimization programming and solved by adaptive particle swarm optimization (APSO), which has higher accuracy and speed than the usual PSO algorithm. Besides these, the participation factor (PF) method is used to select the most appropriate location for the DC-PSS installation. Finally, the effects of DC-PSS are studied in small-signal modelling and frequency response analysis. The main differences between this article and [17] are listed as follows. The main purpose of [17] is to introduce a method for optimal location of the stabilizer in a VSC-based grid, which used π-model to transmission line modelling. But here, the FD-π model will be used for transmission line modelling. The authors in [17] have proposed a method to improve voltage oscillations that is installed on the DC side of the VSC-HVDC, however here DC-PSS will be used on the DC side of the MMC-HVDC. The proposed controller is compared with the controller based on conventional PI and droop, and the results of this comparison are discussed in detail. The PSO algorithm is used in [17] to optimize the parameters, but here, the APSO algorithm is employed to optimize the parameters.

The main contributions of the current study are as follows:

- introducing an effective direct voltage damping controller as DC-PSS applied to the DC side of MMC-HVDC stations, to deal with negative effects of large DC reactors on direct voltage and power and improve the overall MT-HVDC system direct voltage/power stability;

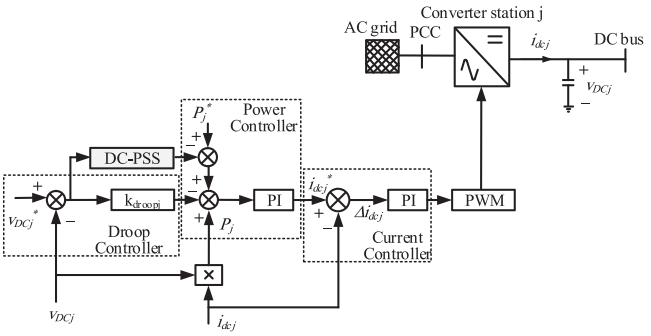

FIGURE 1 Structure of V-P droop controller for an HVDC station

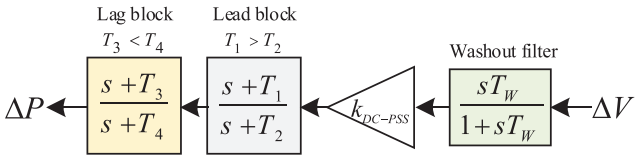

FIGURE 2 The general structure of DC-PSS

- employing direct voltage/power stability alongside the droop controller to make proper power-sharing while improving stability;
- tuning of the parameters of DC-PSS by the APSO algorithm to eliminate direct voltage fluctuations considering MMC-HVDC and FD-π line modelling;
- selecting the appropriate location for the installation of DC-PSS.

The remaining sections of the paper are organized as follows. In Section 2, the proposed control strategy is presented and analysed. Section 3 discusses the optimization approach. Small-signal stability analysis is investigated in Section 4. Simulation results are reported in Section 5.

2 | PROPOSED CONTROL STRATEGY

Because of the lack of inertia, the low-frequency oscillatory modes of HVDC grids are less damped out than those in AC power systems. This paper proposes a method, that during the transient conditions, DC voltages of the HVDC grid will be controlled by providing transient damping. In this method, *V-P* droop control is equipped with a supplementary signal to improve the stability of the HVDC grid which is supplied through DC-PSS. As in the AC power system, the PSS improves the dynamic performance of the power system by adding auxiliary signals to the excitation system [5], a DC-PSS as a damping controller in DC system, operates analogous to a PSS in an AC system and by injecting an additional signal, improves the stability of the HVDC grid. A general control structure of such a controller is presented in Figure 1 The structure of the proposed DC-PSS is shown in Figure 2 In this structure, the locally measured voltage is used as the input that indicates the power balance index in the HVDC grid. This stabilizer produces an

auxiliary damping signal in the output that is proportional to the input signal. Conventional PSS, as a lead-lag compensator is mainly designed based on using a linear model and considering one operating point [5].

As Figure 2 shows, DC-PSS consists of four blocks: a lead compensator block (with $T_1 > T_2$) to improve the speed response and reduce the transient oscillation peak, a lag block (with $T_3 < T_4$) to improve steady-state response, a gain block to determine the amount of damping created by DC-PSS, and a washout block. The gain value $k_{DC\text{-}PSS}$ determines the amount of damping created by DC-PSS. Ideally, the interest rate is adjusted to a value corresponding to the maximum damping, however, its value is usually limited by other considerations. The washout filter block acts as a high-pass filter with a time constant T_W that allows signals corresponding to voltage fluctuations to pass unchanged. The wash filter only allows direct voltage fluctuations to be transmitted and filter the steady-state offset in the output, without allowing the damping controller to react to a dynamic exceeding a certain frequency threshold. The proposed stabilizer on the active power loop is fed by voltage deviations (ΔV). As is usually the PSS input signal in generator systems is speed deviation, the measured local DC voltage in the DC system, is the DC-PSS input. As a result, its output is proportional to the power oscillations. In the steady-state conditions, an onshore HVDC station equipped with the DC-PSS behaves similarly to a conventional converter with active power control mode.

3 | OPTIMIZATION APPROACH

3.1 | Objective function

Parameters of the proposed stabilizer are optimally tuned at the same time by the APSO algorithm. The objective function (1) defines the E_{DC} parameter as an error criterion [18]. This objective function calculates the area under the voltage curve following oscillations and must be minimized. As shown by (1), actually this objective function calculates the error criterion for the sum of the buses from 1 to n. It means that E_{DC} for each DC bus is the region in the plane that is bounded by the graph of DC voltage and proportional to oscillations of direct voltage. Therefore, by minimizing E_{DC} the oscillations can be reduced. In (1), the main reason to include t (time) as the study time limit, in the integration criterion is that the fault severity is considered in the parameter optimization and the parameters can be optimized in such a way that the effect of DC-PSS to be greater in the initial moments of fault. In this equation, n represents the number of busses. Accordingly, the goal here is to minimize the E_{DC} parameter as defined in the following:

$$E_{DC} = \sum_{b=1}^{n} \left(\int_0^t t \left| \Delta V(t)_{DC(b)}(t) \right| dt \right) . \tag{1}$$

The advantage of this objective function is that minimal dynamic information is required to calculate E_{DC}, and it is only necessary to measure the voltage deviation per bus instead of identifying the model parameters required for the DC-PSS design. However, the problem of optimization of the parameters requires special constraints that are all related to the limits of each of the values and should be taken into account. The objective function, (1), should be minimized considering the maximum and minimum of each parameter. The definition of the objective function in this way indicates that if there is no error or perturbation in the system, the value of this function is zero.

3.2 | APSO algorithm

An APSO algorithm is used to solve the optimization problem. The APSO algorithm has many advantages over the classic PSO algorithm. These advantages include a global search across the search space at a higher convergence rate [10]. Its details and the solution methodology are presented and discussed in [10].

Since updating the speed and position of each particle is determined based on the objective function, it is very important to select the appropriate objective function. The process of optimizing the parameters here is summarized in the following steps.

Step 1. The population is initialized. At the current position, the mean distance of each particle to all the other particles is calculated. The globally best particle is defined as d_g. All d_i's are compared and determine the maximum and minimum distances $d_{\max}$ and $d_{\min}$. Then, an 'evolutionary factor' f is calculated. Finally, f is classified into one of the several sets. Also, in each subpopulation, a specific set of motion coefficients (c_1, c_2) are used, which for each subpopulation change adaptively during optimization. Finally, the most optimal solution that is produced is considered. Several particles are selected as a population using a random probability distribution function in a space with dimensions corresponding to the number of parameters. The weighting or inertia coefficient of the algorithm is adjusted proportionally to the number of iterations of the algorithm to result in an adaptive algorithm and find better answers. In addition, the properties of other algorithms such as genetic algorithms (GAs) are also used in the algorithm to obtain the modified algorithm. The balance between the global and local search capabilities in the PSO algorithm is shown by inertia weight ω, that it can be large in exploration mode and small in exploitation. However, reducing ω overtime is not necessarily correct. Therefore, (2) can be defined in such a way that the value of $\omega(f)$, according to the amplitude of changes f, relatively large in the exploration mode and relatively small in the convergence mode [10].

$$\omega(f) = \frac{1}{1 + 1.5e^{-2.6f}} , \ \forall f \in [0, 1] . \tag{2}$$

Consequently, ω adapts to the search environment characterized by f. This means that in exploration mode, large f and ω are in favour of global search, and when f is small, an exploitation

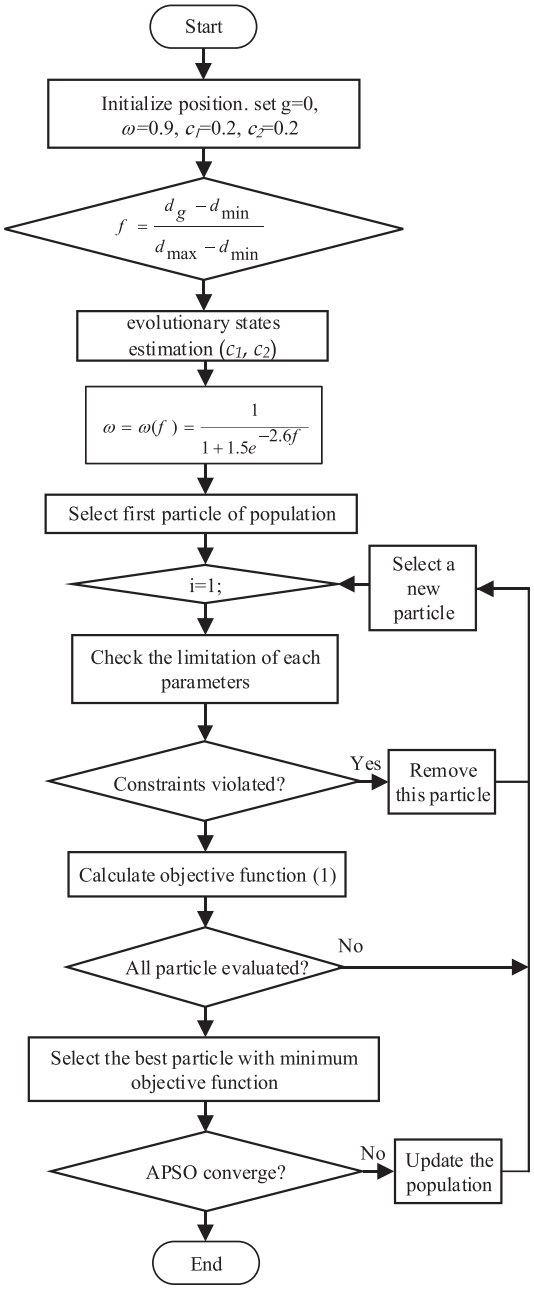

FIGURE 3 Adaptive parameters control process

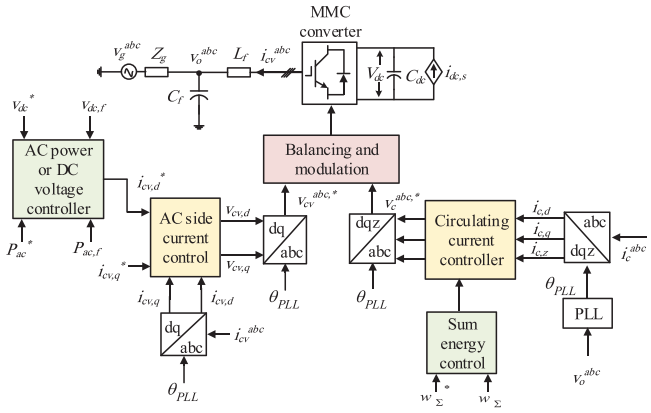

FIGURE 4 MMC model including its control structure

or convergence mode is detected, and hence, ω is reduced to reduce local search.

Figure 3 shows the process of adaptive parameter control for step 1. The initial ω is 0.9. To pull each particle to the best position, the c_1 parameter is considered, and to push the norms to the faster convergence of the region, the c_2 parameter is considered. Also, g is in the best position in the neighbourhood. It is assumed that the initial of both of these values is 0.2.

Step 2. In this step, after randomly selecting a particle and calculating the value of each parameter, the minimum and maximum limits for each parameter are checked, and then the E_{DC} criterion is calculated.

Step 3. The position (parameter) of each particle compares with its previous value and the better particle is selected.

Step 4. The evolution rate and the degree of adaptive aggregation are calculated and the speed and position information for each particle is updated.

Step 5. The criterion stops according to the maximum number of repetitions of irritation or desired fitness, if the desired repetition time or fitness does not correspond to the stop criterion, goes to the previous step, otherwise, the calculated parameters are recorded as results.

4 | STABILITY ANALYSIS OF HVDC GRID WITH DC-PSS

4.1 | MMC modelling

Figure 4 illustrates the arm switching function model of a modular multi-level converter (MMC), to utilize the state-space model of MMC. This model has the most applications in terms of accuracy and velocity of calculations and it is an appropriate model for transient analysis [19]. However, the detailed IGBT-based model of MMC, due to its very low computational speed and high accuracy is used only to investigate and estimate losses. Also, the averaged value model (AVM) MMC model is not used in transient DC studies, since it has an incorrect response to DC side faults [19]. In this type of modelling, considering the concept of a half-bridge converter switching performance, each MMC arm can be assumed average. The dynamics of such a system can be shown as follows.

4.1.1 | Internal variables modelling of MMC variables

The MMC control system shown in Figure 4 consists of two PI control loops that are modelled by only the sum of the energies and the zero-sequence circulation current as of the internal variables of the MMC. The aggregate energy is controlled by a PI controller in an external control loop. This controller

provides zero-sequence circulating current reference as shown in (3), where, $k_{pw,\Sigma}$ and $k_{iw,\Sigma}$ are the gains of PI controller.

$$\begin{aligned} i^*_{c,z} &= k_{pw,\Sigma}\left(w^*_\Sigma - w_\Sigma\right) + k_{iw,\Sigma}k_\Sigma, \\ \frac{d}{dt}k_\Sigma &= w^*_\Sigma - w_\Sigma. \end{aligned} \tag{3}$$

The internal loop PI controller, controls the internal circulating current of the zero sequence, to form a corresponding reference voltage value $v^*_{c,z}$ in (4). The k_{ffdc} as the coefficient of performance of the feedforward loop has a number between zero and one, if the controller has a feedforward loop, the value of k_{ffdc} is one and otherwise it is zero.

$$\begin{aligned} v^*_{c,z} &= -k_{pc,z}\left(i^*_{c,\Sigma} - i_{c,z}\right) - k_{ic,z}\xi_z + k_{ffdc}v_{DC}, \\ \frac{d}{dt}\xi_z &= i^*_{c,z} - i_{c,z}. \end{aligned} \tag{4}$$

4.1.2 | AC side electrical modelling

The current controller loops and phase-locked loop (PLL), relevant to the AC side of the MMC converter, can be modelled like the AC side modelling of VSC converters [19]. In the following equations, i_{cv} is the converter side current, i_o is the grid side current, and v_o is equivalent capacitor voltage.

$$\frac{d}{dt}i_{cv} = -\left(\frac{\left(\frac{r_a}{2} + r_f\right)\omega_b}{\frac{L_a}{2} + L_f} + j\omega_g\omega_b\right)i_{cv} + Av_{cv} - Av_o, \tag{5}$$

$$A = \frac{\omega_b}{\frac{L_a}{2} + L_f}, \tag{6}$$

$$\frac{d}{dt}v_o = -j\omega_g\omega_b v_o + \frac{\omega_b}{C_f}i_{cv} - \frac{\omega_b}{C_f}i_o, \tag{7}$$

$$\frac{d}{dt}i_o = -\left(j\omega_g\omega_b + \frac{r_g\omega_b}{L_g}\right)i_o - \frac{\omega_b}{C_f}v_g + \frac{\omega_b}{C_f}v_o, \tag{8}$$

where, ω_g is the per-unit grid frequency and L_a, r_a, L_f, r_f, l_g, r_g, C_f are the resistances, capacitance, and inductances of the system. The AC side currents of the converter are controlled by decoupled PI controllers corresponding to the d and q axes. The equations of these controllers are defined by (9–12).

$$k_{ffv}v_o - v^*_{AD} + k_{pc}\left(i^*_{cv} - i_{cv}\right) + k_{ic}\gamma + jL_f\omega_{PLL}i_{cv}, \tag{9}$$

$$\frac{d}{dt}\gamma = i^*_{cv} - i_{cv}, \tag{10}$$

$$v^*_{AD} = k_{AD}\left(v_o - \varphi\right), \tag{11}$$

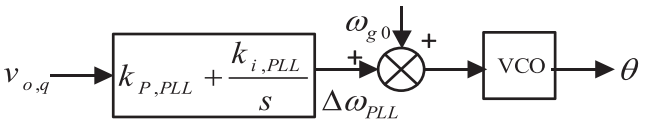

FIGURE 5 PLL linear model

$$\frac{d}{dt}\varphi = \omega_{AD}\left(v_o - \varphi\right). \tag{12}$$

The k_{ffv} as the coefficient of performance of the feedforward loop has a number between zero and one, if the controller has a feedforward loop of v_o, the value of k_{ffv} is one and otherwise it is zero. Also, v^*_{AD} is used to eliminate LC oscillation. In (8), φ is the state of a filter.

4.1.3 | PLL structure

Figure 5 exposes the configuration of PLL, which consists of a PI controller. The linear equations of PLL are described in (13) and (14).

$$\frac{d}{dt}\theta_{PLL} = k_{p,PLL}v_{o,q} + x_{PLL}, \tag{13}$$

$$\frac{d}{dt}x_{PLL} = v_{o,q}. \tag{14}$$

4.1.4 | DC side electrical modelling

State variables of DC side electrical modelling are shown by the next equations.

$$\frac{d}{dt}v_{DC} = \frac{\omega_b}{C_{dc}}\left(i_{dc,s} - 4i_{cz}\right), \tag{15}$$

$$\frac{d}{dt}v_{DC,f} = \omega_{dc,f}\left(v_{DC} - v_{DC,f}\right), \tag{16}$$

where the crossover frequency of the low-pass filter is shown by ω_{dcf}. The control system is such that the AC power defined by (17) and (18) passes through the low-pass filter before being used in the power control loop as shown in (15) and (16).

$$P_{ac} = v_{o,d}i_{cv,d} + v_{o,q}i_{cv,q}, \tag{17}$$

$$\frac{d}{dt}P_{ac,m} = \omega_{pac}\left(P_{ac} + P_{ac,m}\right). \tag{18}$$

The reference current $i^*_{cv,d}$ is defined by PI controller of power and a DC voltage droop determines the AC power reference as it is expressed in (19) and (20).

$$i^*_{cv,d} = k_{pp,ac}\left(P^*_{ac} - P_{ac,m}\right) + k_{ip,ac}\rho, \frac{d}{dt}\rho = P^*_{ac} - P_{ac,m}, \tag{19}$$

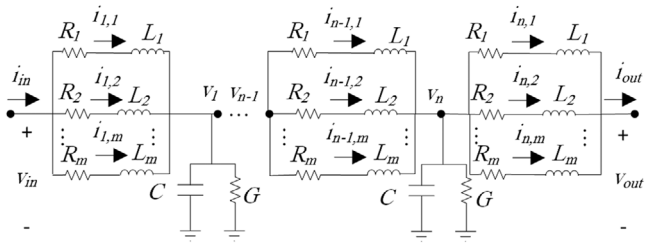

FIGURE 6 FD-π model of lines

$$P_{ac}^{*} = k_{droop}\left(v_{DC}^{*} - v_{DC,f}\right) + P_{ac}^{ref}. \tag{20}$$

According to the above equations, the matrix of state variables is expressed in (21) and the input matrix is expressed in (22).

$$x_j = \left[v_{od}\ v_{oq}\ i_{cv,d}\ i_{cv,q}\ \gamma_d\ \gamma_q\ i_{o,d}\ i_{o,q}\ \varphi_d\ \varphi_q\ v_{DC}\ v_{PLL,d}\ v_{PLL,q}\ v_{DC,f}\ \rho\ p_{ac,m}\ i_{c,\Sigma}\ k_{\Sigma}\ \xi_{\Sigma}\ w_{\Sigma}\right]^{T}, \tag{21}$$

$$u_j = \left[v_{DC}^{ref}\ P_{ac}^{ref}\ i_{cv,q}^{*}\ \left|v_g\right|\ i_{dc,s}\ w_{\Sigma}^{*}\right]^{T}. \tag{22}$$

The equivalent state variables are described as shown in (21). The matrices related to $\Delta v_{DC(j)}$ and $\Delta i_{dc(j)}$ are mined to enable the integration of the MMC model and the HVDC grid model [3] as is shown in (23) and (24).

$$\dot{x}_j = A_j x_j + B_{dj} x d_j + \left[B_{jG}\ B_j\right]\begin{bmatrix}\Delta i_{dc(j)} \\ \Delta P_j^{*}\end{bmatrix}, \tag{23}$$

$$\Delta v_{DC(j)} = C_{jG} x_j. \tag{24}$$

4.2 | DC network model

The conventional π-section model of a line accurately shows the cable behaviour only at a single point of the frequency domain.

Instead, the frequency-dependent π model can be used to modelling the behaviour of cables in a specific frequency range. The FD- π model consists of a lumped circuit with parallel *R-L* branches in each section of the π model of the line. The accuracy and validity of the FD- π model are determined by the number of sections of the π model and the number of parallel branches in each section. In the π-section model, the number of sections improves hyperbolic factors, but does not necessarily lead to a good approximation of the actual behaviour of the cable because it does not allow the frequency dependence of the distributed parameters to be considered [15]. In order to the modelling of line based on FD-π, firstly the line is divided into *n* sections. The number of sections is determined by the length of the line and the frequency range to be interested. Then the number of parallel lines is considered and specified. Figure 6 shows the line model based on FD-π [16]. The number of the parallel branch is showed by *m*. Then, the state-space model of the *j*th line and the related DC breaking reactors:

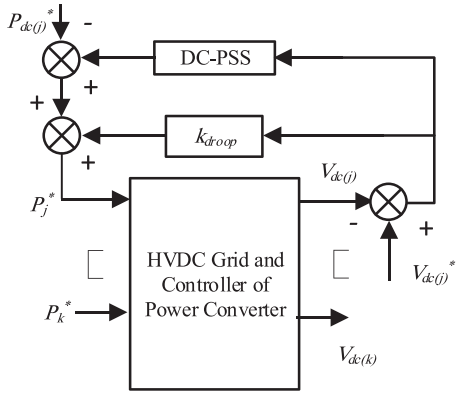

FIGURE 7 Closed-loop model of a typical HVDC grid with the proposed supplementary stabilizer

$$[\dot{x}] = \left[A_j^{line}\right][x] + \left[B_j^{line}\right][u], \tag{25}$$

$$y = \left[c_j^{line}\right][x], \tag{26}$$

where the input is DC voltages at the two ends and the output is DC currents out of them as output:

$$[x] = \left[V_1\ V_2\ \ldots\ V_n\ i_{in}\ i_{l1}\ \ldots\ i_{l(n)}\ i_o\right]^{T}, \tag{27}$$

$$[Y] = \left[i_{in}\ i_{out}\right]^{T},\ [u] = \left[V_{in}\ V_{out}\right]^{T}. \tag{28}$$

For an HVDC grid, the models of DC line (25) and (26) can be unified to make the state-space model of the general DC grid with m separate line [14]. To obtain a proper input vector of the line model, V_{tr} is employed to convert the vector of the DC voltages of MMC terminal and for obtaining a direct current from the line model outputs, and I_{tr} is employed to attain the direct current vector of the converter from the line model outputs, as exposed in (29) and (30) [3].

$$\left[V_{DC(1)}\ \cdots\ V_{Dc(n)}\right]^{T} = V_{tr}^{-1}\left[V_{in}^{line(1)}\ V_{out}^{line(1)}\ \cdots\ V_{in}^{line(m)}\ V_{out}^{line(m)}\right]^{T}, \tag{29}$$

$$\left[i_{dc(1)}\ \cdots\ i_{dc(n)}\right]^{T} = I_{tr}^{-1}\left[i_{in}^{line(1)}\ i_{out}^{line(1)}\ \cdots\ i_{in}^{line(m)}\ i_{out}^{line(m)}\right]^{T}. \tag{30}$$

4.3 | Droop controller and DC-PSS modelling

Figure 7 shows a closed-loop model of a typical HVDC grid with a proposed supplementary stabilizer. As is shown in Figure 7 for modelling a droop controller and supplementary stabilizer in converters equipped with this type of controller, it is sufficient to write the reference power according to the droop gain and in terms of DC voltage.

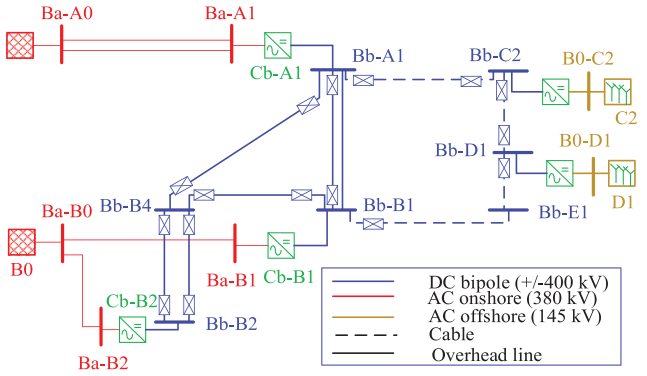

FIGURE 8 Cigré DCS3 test HVDC grids

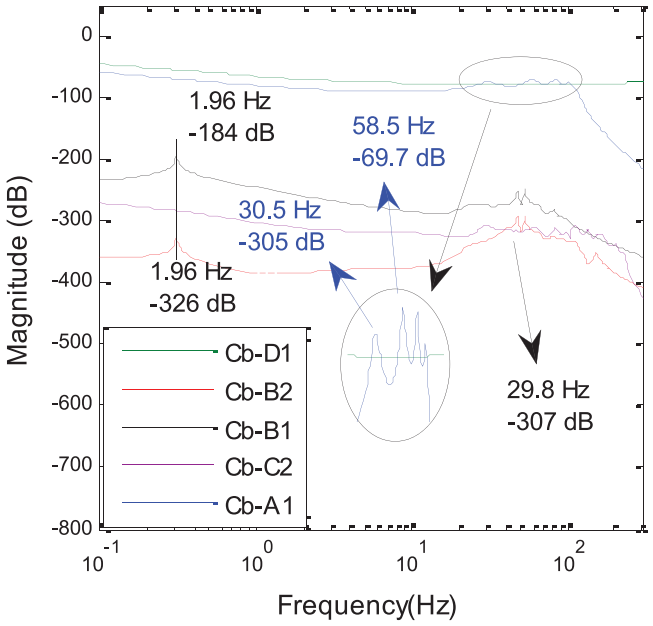

FIGURE 9 The singular value plot of the closed-loop models with all the DC voltages and P_1^* ($k_{droop1} = 0.3$; Cb-B2: $k_{droop2} = 0.42$)

4.4 | MMC modelling alongside DC network modelling

DC grid state-space model considering the MIMO plant model of the grid expressed as:

$$\dot{x}_G = A_G x_G + B_G \Delta V_{DC}\ \Delta i_{dc} = C_G x_G. \tag{31}$$

By combing the investigative models of MMCs of all terminals and the HVDC network model, the state-space model can be shown in (31) [3]. Where x_j is the state variable of the jth converter, B_{Gj} is the jth column of B_G, and C_{Gj} is the jth row of C_G, n is the entire number of the power converters, n_G is the number of state variables of x_G.

5 | SIMULATION RESULTS

5.1 | Network under study and its modelling

Cigré DCS3 test HVDC grid is selected for the investigation of the proposed control strategy [20]. It should be mentioned that the standard test network (Cigre DCS3) is only opted as an illustrative test case and the proposed strategy can also be easily applied to any other selected VSC-based HVDC grids. The main goal is to improve the direct voltage stability and decreasing power variations in the events of transients and this standard grid is selected to confirm the performance and eligibilities of our proposed control strategy. The rated power and voltage for each converter are 1000 MW and ±320 kV. Moreover, it is also assumed that the system has a symmetrical monopole topology. It should be noted that, in line modelling, the number of sections of each line and the number of parallel branches determine the modelling accuracy for each specific frequency range. So, here, it is assuming that number of sections to model a DC line is $n = 10$ and the number of the parallel branch of each section is $m = 5$ [15]. See Figure 8 illustrates the Cigré DCS3 test HVDC grids.

In this study, the transmission lines are modelled by FD-π model [15].

5.2 | Optimal placement of DC-PSS

The PF analysis is used to select the proper location for the DC-PSS installation [20].

This method can also be applied to identify the suitable placement of droop control. The singular value technique is the corresponding frequency response in the system with multivariable control systems and offers perceptive evidence about gains among various output and input [21]. Moreover, the method of optimal placement is working to measure the gain among the reference of power related to a specific MMC terminal and direct voltages of all the terminals. A plot of singular value displays the gains amongst the output and that of the input vector in the frequency domain [21]. The suitable terminal for the installation of DC-PSS is a terminal with large single values in the specified frequency range. Figure 9 shows the plot of the singular values of the power set-point of the selected terminals and output voltage vector for the closed-loop model with data from [22].

PF method investigation has been accepted for the selected optimal placement of PSS in each multi-machine system [23].

Among the five terminals of the system, two terminals equipped with the droop controller were selected as a candidate for DC-PSS installation. Table 1 shows the calculated PFs equivalent to the low-frequency poorly damped modes for the two terminals with droop controller, concerning the voltage of the station. Cb-B1 is selected as the anticipated power converter station for the installation of DC-PSS, due to its significant participation in the most poorly damped mode. Corresponding to this method, the desired power converter station for the installation of DC-PSS is Cb-B1.

TABLE 1 Participation factors for the two selected terminals

Frequency (Hz)	Eigenvalue	Cb-B1	Cb-B2
1.96	−12.3 ± 0.0132i	0.5679	0.3125
2.16	−13.4 ± 0.0131i	0.9679	0.2102
30.7	−17.9 ± 30.1i	0.3215	0.2618
35.9	−17.9 ± 30.1i	0.2112	0.1894

TABLE 2 Optimal parameters of DC-PSS found by APSO

Parameter	Minimum	Optimal value	Maximum
K_{DC}	100	123.1	150
T_1	0.01	0.0211	0.1
T_2	0.01	0.01	0.1
T_3	0.01	0.0012	0.1
T_4	0.01	0.01	0.1

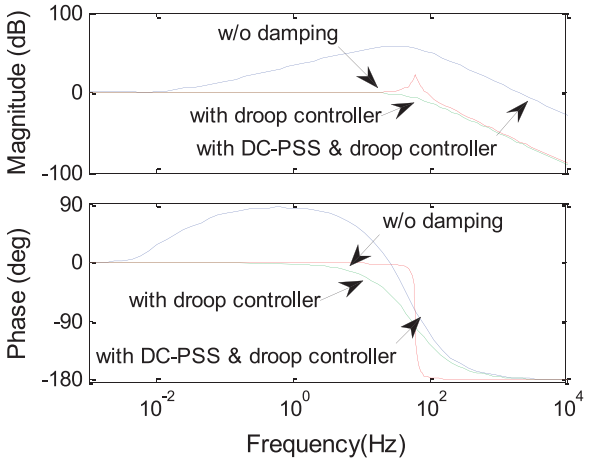

FIGURE 10 Root locus and bode plots of the $vj(s)/vj^*(s)$ transfer function with $k_{droop} = 0.3$ from a single converter

5.3 | Optimization parameters of DC-PSS

APSO algorithm is used to optimize DC-PSS parameters in HVD grid. The parameters T_1, T_2, T_3, T_4, and $k_{DC\text{-}PSS}$ are optimized by considering the grid stability and minimizing the E_{DC} criterion in (1).

Based on the analysis presented in Section 3.2, the proper values of the DC-PSS parameters were obtained from the APSO listed in Table 2

For robustness of the solutions, the obtained values of E_{DC} by employing the calculated parameters of the GA and the APSO algorithm are compared following several faults. The results of this comparison are shown in Table 3 As the table shows, the proposed APSO algorithm achieves a better response than the GA algorithm, it also has a faster response and fewer repetitions.

5.4 | Dynamic stability analysis

The bode plots of the transfer function between voltage reference v_j^* (s) and the local direct voltage v_j (s), which can be straight mined from the MIMO model, without any damping method, with droop controller, and employing DC-PSS beside droop, are illustrated in Figure 10 This plot shows that the DC-PSS and droop controller work at the resonant frequency, but it is clear that DC-PSS gives a higher bandwidth, which improves the transient response and reduces the amount of mutation. Besides, this figure shows that DC-PSS gives a higher phase margin at low frequency. Therefore, the designed compensator will provide more proper damping to the system.

TABLE 3 Comparison of E_{DC} calculated by the parameters obtained from two algorithm

	APSO		GA	
	E_{DC}	Rep.	E_{DC}	Rep.
Three-phase short circuit	0.091	83	0.098	100
Decreasing load	0.283	79	0.297	100
Increasing load	0.287	81	0.296	100

5.5 | Investigation of the proposed DC-PSS for the understudy network

In this section, the proposed DC-PSS on the HVDC test system is examined. As mentioned before in this study Cigré DCS3 is selected and MATLAB/SIMULINK is used for the simulations. Responses of the DC voltage and DC power of V_{DC}-Cb-A1, V_{DC}-Cb-B2, V_{DC}-Cb-B1 and P_{DC}-Cb-A1, P_{DC}-Cb-B2, P_{DC}-Cb-B1 under 200 MW reducing of generation in wind farm 2 and during fault happening for 10 ms (3–3.01 s) in Cb-A1 bus with droop controller at Cb-B1 and Cb-B2 ($k_{droop} = 0.3$, $k_{droop} = 0.2$) following with and without DC-PSS is shown as follows. However, despite the DC-PSS on the Cb-B1 and the use of power fluctuations to reduce voltage fluctuations, the power of this bus increases slightly in the initial moments of the fault.

5.6 | Reducing of generation

Figure 11(a) shows that the presence of DC-PSS along with droop controller reduces the oscillation of voltage at the instant of generation decrease and increases the speed of getting the steady-state condition. Furthermore, Figure 11(b) illustrates that the damping of voltage fluctuations has led to a reduction of power oscillations and increases the speed of getting the steady state for power.

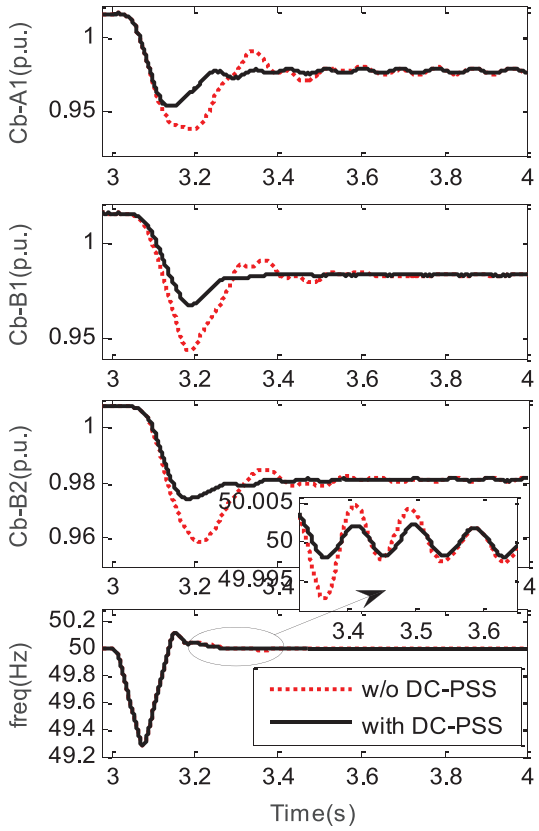

(a) Frequency and direct voltage of Cb-A1, Cb-B2 and Cb-B1.

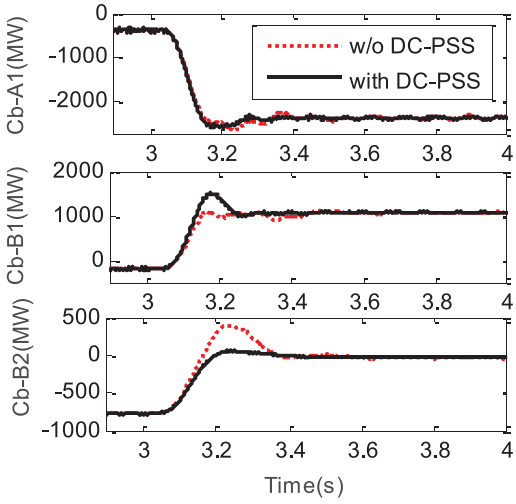

(b) Power of Cb-A1, Cb-B2 and Cb-B1

FIGURE 11 Frequency, DC voltage and DC power of Cb-A1, Cb-B2 and Cb-B1 following 200 MW reducing of generation in wind farm 2. (a) Frequency and direct voltage of Cb-A1, Cb-B2 and Cb-B1. (b) Power of Cb-A1, Cb-B2 and Cb-B1

5.7 | Fault incidence at Cb-A1

Figure 12 shows V_{DC}-Cb-A1, V_{DC}-Cb-B2, and V_{DC}-Cb-B1 profiles during fault occurrence for 10 ms (3–3.01 s) in Cb-A1 bus. The fault at Cb-A1, resulted in a 70% voltage drop. Since it is revealed from Figure 12 throughout the fault, the DC-PSS has been able to minimize the voltage peak and stabilize the bus

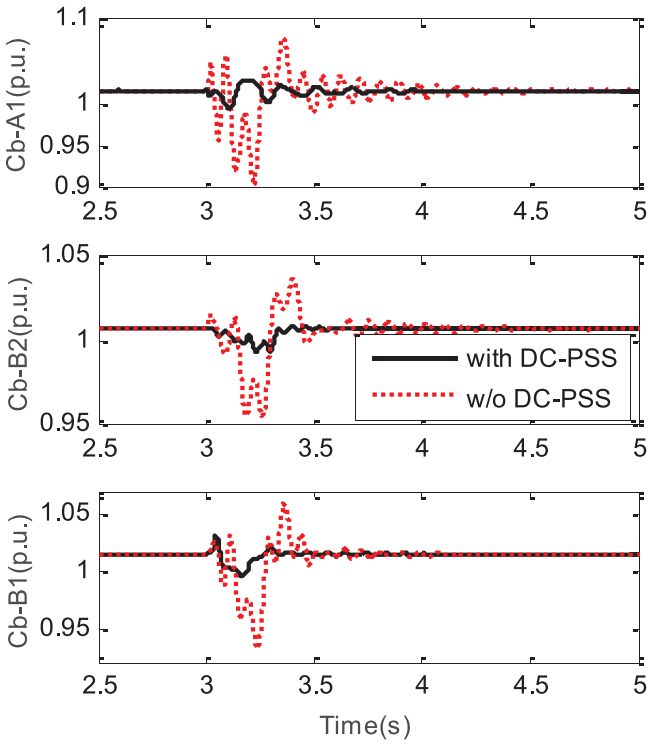

FIGURE 12 The DC voltage of Cb-A1, Cb-B2, and Cb-B1 following a fault happening at Cb-A1

voltage faster and it means that the peak of voltage has been improved.

Figure 12 confirms that without DC-PSS, the peak voltage may be large, so that it goes out of range and the protection system enters operation. In addition, this figure shows that under the same condition proposed, the method with DC-PSS after elimination of the fault has been able to bring back the value of the voltage to the previous value with a smaller peak and less oscillation. The comparison of the simulation results in Figure 12 shows the damping improvement by the proposed DC-PSS.

Figures 11(a) and (b) in addition to displaying voltage and power fluctuations, show that the damping signal does not affect the performance of the droop controller and does not prevent its proper operation. This means that, despite the washout filter, the injection signal is applied only at the period of disturbances. Figure 11(a) also shows that the use of DC-PSS has an effect on the frequency and DC-PSS can also improve frequency oscillations. Because in the weak systems, usually if the frequency drops reach below 0.98 pu (or 49 Hz in 50 Hz power systems) the load shedding will be activated. As can be seen from Figures 11(a) and (b) the proposed method not only reduces the oscillations but also does not enable load shedding.

Additional signals from DC-PSS will reduce power fluctuations and cause a faster decrease in power fluctuations.

Table 4 shows the improvement of the damping by the results of the analytical study, if DC-PSS is on Cb-B1. The impact of DC-PSS in Cb-B1 on the oscillating frequency and the damping ratio ζ of the closed-loop MIMO model for the poorly damped

TABLE 4 Low-frequency modes with and without the proposed damping controller (for Cb-B1)

Without DC-PSS		With DC-PSS	
Freq.	**Damping ζ**	**Freq.**	**Damping ζ**
1.96 Hz	0.00143	2.6 Hz	0.4301
8.75 Hz	0.00133	9.84 Hz	0.3603
11.43 Hz	0.00421	14.53 Hz	0.1220
23.1 Hz	0.0136	21.8 Hz	0.0377

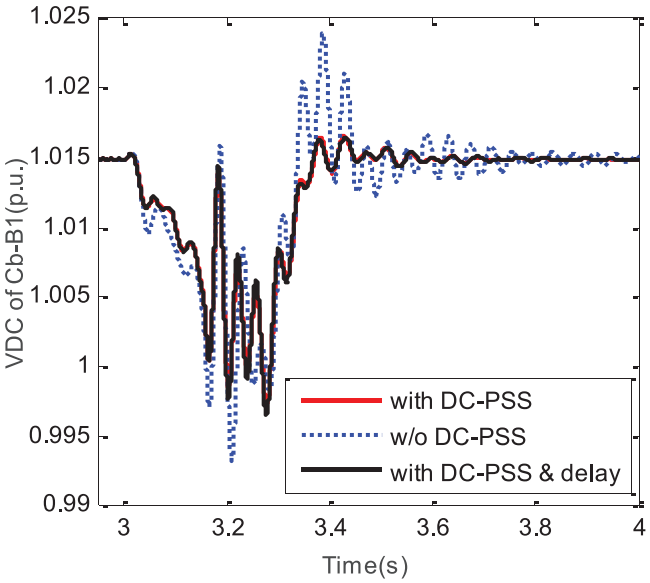

FIGURE 13 Direct voltage of Cb-B1 following three-phase short circuit in the AC side of Cb-A1 with the delay time

modes are intended. As the location of the DC-PSS is chosen to aim the low-frequency modes with the damping, the damping of each mode by DC-PSS is enhanced most intensely. Besides, the DC-PSS has a completely supportive effect on the damping of a range of frequencies and also increases the stability margin.

5.8 | The effect of time delay on the performance of DC-PSS

Figure 13 shows V_{DC} of Cb-B1 profiles during fault occurrence for 150 ms (3–3.15 s) in Cb-A1 bus. The fault at Cb-A1, resulted in a three-phase short circuit in the AC side of Cb-A1. Since it is revealed from Figure 13 throughout the fault, the DC-PSS with time delay for 1.1 ms [24] and without time delay has been able to minimize the voltage peak and stabilize the bus voltage faster and it means that the peak of voltage has been improved. However, if the system is operated without time delay, the system response will improve slightly. The DC-PSS uses a local signal, however, Figure 13 shows that the DC-PSS with remote signals as inputs, with a time delay of 1.1 ms has also acceptable performance.

6 | CONCLUSION

The inclusion of DC-PSS to the traditional droop control has been suggested to improve the dynamic performance and small-signal stability of the direct voltage control in HVDC grid. The proposed DC-PSS has been evaluated on Cigré DCS3 test HVDC grid using pole-zero plot, analytical model, and frequency domain analysis. DC reactors reduce the direct voltage control capability and have destructive effects on the dynamic stability of MT-HVDC relative to the power flow variations. In such a system, despite the variety of controllers, the system dynamics are highly sensitive to the operating point, so it is essential to have an additional damping signal. DC-PSS can improve the small-signal stability of the system, which is usually caused by insufficient damping of oscillations. The simulations in the time domain in transient mode and eigenvalue analysis of the test system have confirmed the decent performance of the proposed DC damping controller. In addition, in order to increase the performance of the proposed DC-PSS, suitable methods for optimal design and optimal placement for DC-PSS are presented.

CONFLICT OF INTEREST

The authors declare no conflict of interest.

DATA AVAILABILITY STATEMENT

Data sharing is not applicable to this article as no new data were created or analysed in this study.

ORCID

Hassan Moradi CheshmehBeigi https://orcid.org/0000-0002-4802-6117

REFERENCES

1. Rakhshani, E., Rouzbehi, K.J., Sánchez, A., Tobar, A.C., Pouresmaeil, E.: Integration of large scale PV-based generation into power systems: A survey. Energies 12, 1425 (2019)
2. Rouzbehi, K., Miranian, A., Candela, J.I., Luna, A., Rodriguez, P.: A hierarchical control structure for multi-terminal VSC-based HVDC grids with GVD characteristics. In: **2013** International Conference on Renewable Energy Research and Applications (ICRERA), pp. 996–100 (2013)
3. Heidary, A., Radmanesh, H., Rouzbehi, K., Pou, J.: A DC-reactor-based solid-state fault current limiter for HVdc applications. IEEE Trans. Power Delivery 34(2), 720-728 (2019)
4. Rodriguez, P., Rouzbehi, K.: Multi-terminal DC grids: Challenges and prospects. J. Modern Power Syst. Clean Ener. 5(4), 515-523, (2017)
5. Kundur, Prabha S.: Power system stability. In Power System Stability and Control, pp. 7–1 (McGraw-Hill, New York: 1994)
6. Shah, R., Sánchez, J.C., Preece, R., Barnes, M.: Stability and control of mixed AC–DC systems with VSC-HVDC: A review. IET Gener. Transm. Distrib. 12(10), 2207-2219 (2018)
7. Zhou, Q., Ding, Y., Mai, K., Bian, X., Zhou, B.: Mitigation of subsynchronous oscillation in a VSC-HVDC connected offshore wind farm integrated to grid. Int. J. Elect. Power Energy Syst. 109, 29–37 (2019)
8. Bergna-Diaz, G., Suul, J.A., Berne, E., Vannier, J.-C., Molinas, M.: Optimal shaping of the MMC circulating currents for preventing AC-side power

oscillations from propagating into HVDC grids. IEEE Trans. Emerg. Sel. Topics Power Electron 7(2), 1015–1030 (2019)
9. Zhu, S., Liu, K., Qin, L., Wang, Q., Pu, Y., Li, Q., Wang, S.: Analysis and suppression of DC oscillation caused by DC capacitors in VSC-based offshore island power supply system. IEEJ Trans. Electr. Electron. Eng. 14(4), 545–555 (2018)
10. Zhan, Z.H., Zhang, J., Li, Y., Chung, H.S.H.: Adaptive particle swarm optimization. IEEE Trans. Syst. Man Cyberm. Part B (Cybernetics) 39(6), 1362-1381 (2009)
11. Prieto-Araujo, E., Egea-Alvarez, A., Fekriasl, S., Gomis-Bellmunt, O.: DC voltage droop control design for multiterminal HVDC systems considering AC and DC grid dynamics. IEEE Trans. Power Delivery 31(2), 575–585 (2016)
12. Cole, S., Beerten, J., Belmans, R.: Generalized dynamic VSC MTDC model for power system stability studies. IEEE Trans. Power Syst. 25(3), 1655-1662 (2010)
13. Rouzbehi, K., Miranian, A., Luna, A., Rodriguez, P.: DC voltage control and power-sharing in multiterminal DC grids based on optimal DC power flow and voltage-droop strategy. IEEE Trans. Emerg. Sel. Topics Power Electron. 2(4), 1171–1180 (2014)
14. Wang, W., Barnes, M., Marjanovic, O., Cwikowski, O.: Impact of DC breaker systems on multiterminal VSC-HVDC stability. IEEE Trans. Power Delivery 31(2), 769–779 (2015)
15. D'Arco S., Suul J.A., Beerten J.: Configuration and model order selection of frequency-dependent π models for representing DC cables in small-signal eigenvalue analysis of HVDC transmission systems. IEEE Journal of Emerging and Selected Topics in Power Electronics. 9(2), 2410–2426 (2021). http://doi.org/10.1109/jestpe.2020.2976046
16. Beerten, J., D'Arco, S., Suul, J.A.: Cable model order reduction for HVDC systems interoperability analysis. 11th IET International Conference on AC and DC Power Transmission 10–12 (2015)
17. Azizi, N., Moradi-CheshmehBeigi, H., Rouzbehi, K.: Optimal placement of direct current power system stabilizer (DC-PSS) in multi-terminal HVDC grids. IET Gener. Transm. Distrib. 14(12), 2315-2322 (2020)
18. Khodabakhshian, A., Hemmati, R., Moazzami, M.: Multi-band power system stabilizer design by using CPCE algorithm for multi-machine power system. Electric Power Syst. Res. 101, 36-48 (2013)
19. Saad, H., Dennetière, S., Mahseredjian, J., Delarue, P., Guillaud, X., Peralta, J., Nguefeu, S.: Modular multilevel converter models for electromagnetic transients. IEEE Trans. Power Delivery 29(3), 1481-1489 (2014)
20. Yazdi, S.S.H., Rouzbehi, K., Candela, J.I., Milimonfared, J., Rodriguez, P.: Flexible HVDC transmission systems small-signal modelling: A case study on CIGRE Test MT-HVDC grid. In: IECON 2017-43rd Annual Conference of the IEEE Industrial Electronics Society pp. 256-262 (2017)
21. Prieto-Araujo, E., Bianchi, F.D., Junyent-Ferre, A., Gomis-Bellmunt, O.: Methodology for droop control dynamic analysis of multiterminal VSC-HVDC grids for offshore wind farms. IEEE Trans. Power Delivery 26(4), 2476-2485 (2011)
22. Thams, F., Chatzivasileiadis, S., Prieto-Araujo, E., Eriksson, R.: Disturbance attenuation of dc voltage droop control structures in a multi-terminal HVDC grid. In: 2017 IEEE Manchester PowerTech, pp. 1–6 (2017)
23. Chaudhuri, N.R., Majumder, R., Chaudhuri, B., Pan, J.: Stability analysis of VSC MTDC grids connected to multimachine AC systems. IEEE Trans. Power Delivery. 26(4), 2774-2784 (2011)
24. Kontos, E., Pinto, R.T., Rodrigues, S., Bauer, P.: Impact of HVDC transmission system topology on multiterminal DC network faults. IEEE Trans. Power Delivery 30(2), 844-852 (2014)

How to cite this article: Azizi N., CheshmehBeigi H.M., Rouzbehi K.: HVDC Grids Stability Improvement by Direct Current Power System Stabilizer. IET Gener. Transm. Distrib. 16, 492–502 (2022). https://doi.org/10.1049/gtd2.12295